Journal of Nuclear Materials 378 (2008) 127–133

Contents lists available at ScienceDirect

Journal of Nuclear Materials

journal homepage: www.elsevier.com/locate/jnucmat

Zircaloy-4 cladding corrosion model covering a wide range of PWR experiences

Byung-Ho Lee *, Yang-Hyun Koo, Jae-Yong Oh, Dong-Seong Sohn

Korea Atomic Energy Research Institute, P.O. Box 105, Yuseong, Daejeon 305-600, Republic of Korea

ARTICLE INFO

Article history:
Received 8 August 2007
Accepted 3 April 2008

ABSTRACT

A phenomenological corrosion model for Zircaloy-4 cladding was developed by focusing on the effect of the metallurgy of cladding and the water chemistry combined with the thermo-hydraulic conditions. The metallurgical effect was formulated by considering the Sn content in the cladding and the heat treatment of the cladding. Concerning the effect of the water chemistry, it is assumed that lithium and boron have an influence on the corrosion under the condition of subcooled void formation on the cladding surface. The developed corrosion model was implemented in a fuel performance code, COSMOS, and verified using the database obtained for the UO_2 and MOX fuel rods irradiated in various PWRs. It was elucidated that the corrosion by lithium was enhanced in the case where the fuel rods were irradiated with a high linear power so that a significant subcooled void could be formed on the cladding surface. On the other hand, there was no evidence of the lithium effect even though its concentration was high enough if the void in the coolant was negligible. This result shows that the acceleration of corrosion by an increased lithium concentration occurs only when subcooled voids are formed on the cladding surface. In addition, the comparison between the measurement and the prediction for the MOX fuel rods indicates that no distinguishable difference is found in the corrosion behavior between the MOX and the UO_2 fuels as expected.

1. Introduction

Corrosion of the Zircaloy cladding in PWRs has become more important due to

- a higher fuel discharge burnup to reduce fuel cycle costs,
- a higher coolant inlet temperature to increase plant thermal efficiency, and
- an increase of the coolant pH and lithium concentration to reduce plant radiation levels.

Even though the corrosion mechanism of Zircaloy is still not fully understood as yet, the main factors determining its corrosion rate are the metallurgical characteristics of the cladding, alloy composition, and the irradiation environments of the fast neutron flux, water chemistry, and the thermo-hydraulic condition of the coolant.

Particularly, concerning the water chemistry, an increase in the corrosion rate of ~10–30% has been observed when the maximum coolant lithium content was 2.2–3.5 weight ppm [1,2]. On the contrary, results from some other reports showed no discernible oxidation enhancement in the presence of an elevated lithium concentration [3–5].

Keeping in mind these conflicting corrosion behaviors, a phenomenological corrosion model for Zircaloy-4 cladding was developed to consider the lithium acceleration and boron retardation coupled with the thermo-hydraulic condition of the coolant as well as the metallurgy in the cladding alloy. The developed model after incorporation into the fuel performance code, COSMOS [6], was verified by four cases of various cladding oxidation behaviors for the UO_2 and mixed oxide (MOX) fuel rods irradiated in PWRs.

2. Development of the corrosion model

Since an in-pile fuel performance can be properly predicted with the precise estimation of corrosion behavior of fuel claddings, a phenomenological corrosion model for the cladding in PWRs has been developed and implemented into the fuel performance code, COSMOS [6,7].

In the oxide layer thickness range up to ~2.1 μm (pre-transition range), oxide layer formation has a cubic characteristic. At a layer thickness above ~2.1 μm, there is a change to the linear corrosion kinetics.

The oxidation process of Zircaloy-4 cladding can be estimated using semi-empirical correlations divided into pre-transition and post-transition kinetics. Since the Zircaloy corrosion process is essentially a diffusion-controlled reaction, the Zircaloy oxidation kinetics is characterized by the Arrhenius equation as a function of the temperature, activation energy and additional acceleration factors.

* Corresponding author. Tel.: +82 42 868 8984; fax: +82 42 864 1089.
E-mail address: bholee@kaeri.re.kr (B.-H. Lee).

0022-3115/$ - see front matter © 2008 Elsevier B.V. All rights reserved.
doi:10.1016/j.jnucmat.2008.04.019

The corrosion rate equation in the pre-transition regime is generally given by

$$\frac{d\delta^3}{dt} = K_{pre} \cdot \exp\left(-\frac{Q_{pre}}{R \cdot T_i}\right), \quad (1)$$

$$K_{pre} = F_{Sn} \cdot F_{MPS} \cdot F_{Li,pre} \cdot F_B \cdot F_\phi \cdot F_{pre}, \quad (2)$$

while the oxidation rate in the post-transition regime is given by

$$\frac{d\delta}{dt} = K_{post} \cdot \exp\left(-\frac{Q_{post}}{R \cdot T_i}\right), \quad (3)$$

$$K_{post} = F_{Sn} \cdot F_{MPS} \cdot F_{Li,post} \cdot F_B \cdot F_\phi \cdot F_{post}, \quad (4)$$

where δ is the oxide thickness [mm], t is the time [day], R is the universal gas constant [J/mol-K], T_i is the metal/oxide interface temperature [K], K_{pre} is the frequency factor for pre-transition regime [mm^3/day], K_{post} is the frequency factor for post-transition regime [mm/day], Q_{pre}, Q_{post} is the activation energy for pre-transition and post-transition [J/mol], $F_{Li,pre}$, $F_{Li,post}$ is the enhancement factor due to lithium in the pre-transition and post-transition regime, F_B is the boron retardation factor, F_{Sn} is the Sn (tin) content enhancement factor, F_{MPS} is the second phase particle enhancement factor, and F_ϕ is the fast neutron enhancement factor (>1.0 MeV).

Among the many factors in the corrosion model, we focused on the metallurgical effects such as the annealing and the Sn content of the cladding and the water chemistry (lithium and boron) effect coupled with the thermo-hydraulic condition of the coolant. The differential equation of oxide thickness is solved numerically by a fourth order Runge–Kutta integration formulae [8].

2.1. Metallurgical effects

2.1.1. Sn effect

Sn is one of the most important alloying elements in the cladding. Sn is a solid solution strengthener in the Zircaloy so that it increases its hardness, tensile strength and creep resistance. The standard cladding contains the Sn of 1.2 wt% to 1.7 wt% and the nominal Sn content of Zircaloy-4 cladding is about 1.5 wt%. It has been found that reducing the Sn content in the Zircaloy-4 cladding improves its corrosion resistance although the role of Sn in the oxidation mechanism is not fully understood. This led to the decrease in the Sn content in the Zircaloy-4 cladding. An improved low-Sn cladding shows a reduction in its oxide thickness at high burnups by about 20–40%.

Fig. 1 displays the relative corrosion rate as a function of the Sn content [9]. The corrosion resistance was obviously improved by decreasing the Sn contents. The multiplicative Sn factor can be reasonably fitted with a linear relationship

$$F_{Sn} = -0.2557 + 0.6666 \times SN, \quad (5)$$

where SN is the Sn content in the Zircaloy-4 cladding in wt%.

In addition, by analyzing the measured data [10] of high burnup fuel irradiated in two PWRs, the corrosion ratio of the low Sn to the standard cladding was found to be somewhat distinguishable with a burnup increase, as shown in Fig. 2. The corrosion ratio diminished with the burnup, from 0.82 at a pellet average burnup of 15 MWd/kgU to about 0.6 at 50 MWd/kgU.

Instead of using the burnup-dependent relation, we used a linear relationship of Sn factor which can adequately simulate the Sn effect for the corrosion rate for standard and low Sn claddings after iteratively analyzing the corrosion database. The burnup dependency on corrosion rate would be adopted with more collective database to reveal the clear behavior of corrosion with burnup. It is noted that the Sn factor, F_{Sn}, is normalized to set a value of 1.0 for the cladding with the Sn content of 1.5 wt%.

2.1.2. Annealing effect

The corrosion rate of Zircaloy-4 cladding is affected by the metallurgical variation such as the microstructure, the solute content of the α-matrix as well as the second phase precipitates' size and distribution.

The primary metallurgical factors that have been found to affect the corrosion resistance of the Zircaloy-4 are the size of the second phase precipitates and their distribution. The characteristics of the second phase precipitates are mainly determined by the temperature at which the annealing is performed and a period of time over which the temperature is applied. These two variables are important for manufacturing proper Zircaloy claddings. The combination of these two variables, with more than one heat treatment involved, is termed as an accumulated annealing parameter. The parameter, $(\sum A_i)$, is obtained by

$$\sum A_i = \sum \left[t_i \cdot \exp\left(-\frac{Q}{R \cdot T_i}\right)\right], \quad (6)$$

where t_i is the ith annealing time, T_i the ith temperature of the heat treatment, and Q/R the activation energy divided by the molar gas constant = 40 000 K. It is noted that the annealing parameter is a summation of all applied heat treatments in the α-phase region of zirconium alloys during their fabrication. The annealing parameter is widely used for cladding manufacturing process and it seems to accommodate other variations and their consequent effects on corrosion.

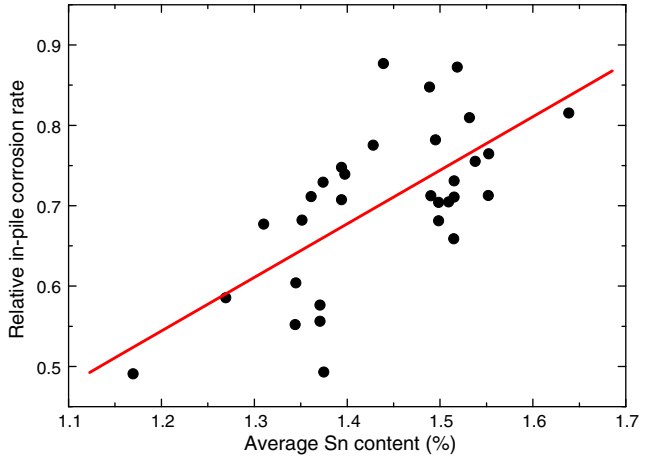

Fig. 1. Sn effect on the relative corrosion rate of the Zircaloy-4 in PWRs [9].

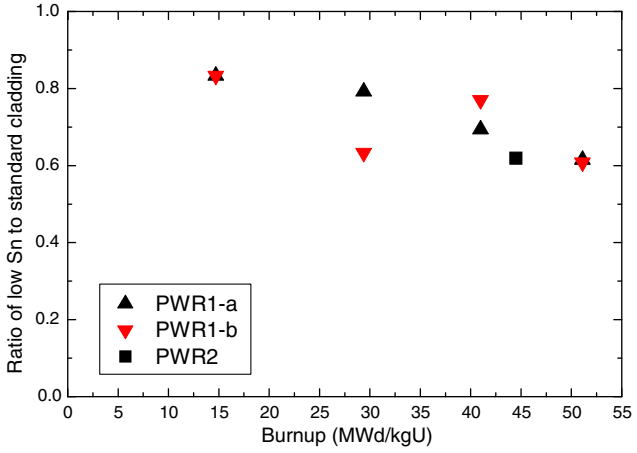

Fig. 2. Corrosion ratio of the low Sn to the standard cladding [10].

Based on the in-laboratory and in-pile measurements of oxide thickness and corrosion rates, the annealing parameter could be reasonably well correlated with the average diameter of second phase precipitates which consequently controls the corrosion behavior of Zircaloys. The average size of these precipitates increases with accumulated annealing parameter as presented in Fig. 3 [9]. The relationship between the mean precipitate size and the annealing parameter was obtained with a trial Logistical formulation as

$$\bar{d}_{\mathrm{MPS}} = 1.58827 - \frac{1.573}{1.0 + \left(\frac{\sum A_i}{7.8818\times10^{-15}}\right)^{0.38504}}, \tag{7}$$

where $\bar{d}_{\mathrm{MPS}}$ is the mean diameter of the second phase precipitates (μm).

Since the physical and metallurgical properties were identified to be responsible for the growth of the collective intermetallic phases present in the alloy as precipitates, the corrosion rate shows the dependency on the average diameter of the precipitates as displayed in Fig. 4.

The metallurgical effect on corrosion is elucidated by considering the dependency of corrosion on the average diameter of the precipitates (Fig. 4) which is related to the annealing parameter (Fig. 3). The multiplicative factor for considering the effect of an average diameter of the precipitates on corrosion rate was fitted with a Gaussian relationship as

$$F_{\mathrm{MPS}} = 1.01425 + \frac{1962.28}{0.15767\cdot\sqrt{2\pi}} \cdot \exp\left(-2\cdot\left(\frac{\bar{d}_{\mathrm{MPS}} + 0.29483}{0.15767}\right)^2\right). \tag{8}$$

In the implementation of the corrosion model into the COSMOS, the F_{MPS} was normalized at a value of 1.0 for the cladding with a mean precipitate size larger than 0.2 μm.

2.2. Water chemistry effect

Lithium hydroxide (LiOH) at a lithium concentration of less than ~2.5 ppm is added into PWRs at startup to maintain the coolant pH within 6.9–7.4. The lithium concentration normally decreases in accordance with a decreasing boric acid concentration and eventually it is reduced to ~0.6 ppm at the end of a fuel cycle when the boron concentration is depleted [9,11]. LiOH also has a function of controlling the corrosion of primary system materials and minimizing the corrosion product transport within the primary system.

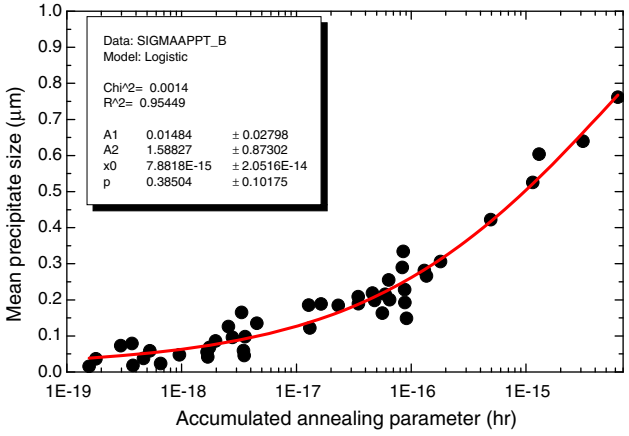

Fig. 3. Intermetallic precipitate size as a function of the accumulated annealing parameter [9].

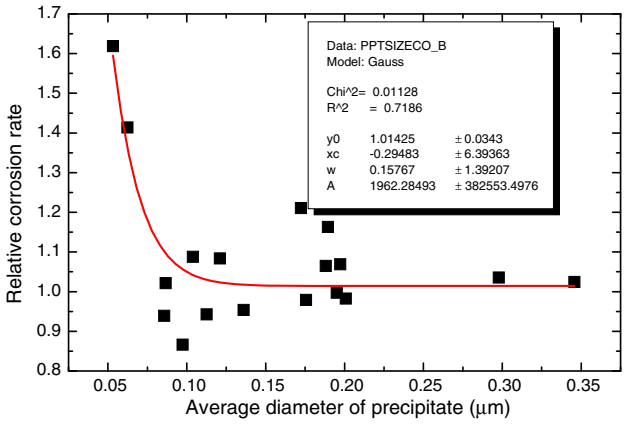

Fig. 4. Relative corrosion rate as a function of the intermetallic precipitate size [9].

Several corrosion tests with various startup concentrations of lithium, ranging form 2.2 to 3.5 ppm, have indicated no easily discernible effect of lithium on Zircaloy cladding corrosion in PWRs. However, it has been reported that some corrosion models from the measured oxidation database have attributed a significant portion of the in-reactor Zircaloy cladding corrosion to the enhancement effect of lithium. The lithium over-concentration occurred under two-phase flow regimes, which resulted in the enhancement of corrosion rate in the Zircaloy-4 cladding [12,13].

Therefore, evidence from these contradictory studies of lithium-related acceleration under a PWR water chemistry condition is somewhat ambiguous.

Even though more experiments and a database on the effect of lithium on the corrosion rate are required, the developed corrosion model postulates the lithium enhanced corrosion rate if enough void is formed on the cladding surface to concentrate the lithium on the oxide surface. Normally, high void fraction does not occur in PWR coolants and, thus, any LiOH enhancement by this mechanism may be less severe. A subcooled boiling is however becoming more common in PWRs with high duty fuel using low leakage core management.

In this regard, the formulation of a lithium history-dependent enhancement factor is explored by analyzing the measured oxidation data which revealed the lithium enhancement by the significant void formation in the coolant.

The formulation of a lithium history-dependent enhancement factor is given by

$$F_{\mathrm{Li}} = \begin{cases} 1.0 & \text{if } \alpha \leqslant \alpha_0 \\ (1+\alpha)\cdot f([\mathrm{Li}], T, C_{\mathrm{f}}) & \text{if } \alpha > \alpha_0, \end{cases} \tag{9}$$

where α is the void fraction, α_0 is the threshold void fraction, C_{f} is the fitting constant, [Li] is the lithium concentration [ppm].

Subcooled void formation can be estimated by using the Levy's subcooled void model [14,15]. Levy's model calculates the true quality in terms of the equilibrium quality and the quality at which a bubble departure starts. The verification of the calculated void fraction was done by a comparison of the results to a thermo-hydraulic code, MATRA [16]. The true quality X_{t} is given by

$$X_{\mathrm{t}} = 0 \quad \text{if } X_{\mathrm{e}} < X_{\mathrm{d}}, \tag{10}$$

$$X_{\mathrm{t}} = X_{\mathrm{e}} - X_{\mathrm{d}}\cdot\exp\left(\frac{X_{\mathrm{e}}}{X_{\mathrm{d}}} - 1\right) \quad \text{if } X_{\mathrm{e}} \geqslant X_{\mathrm{d}}, \tag{11}$$

where X_{e} is the thermodynamic equilibrium quality $\equiv \frac{h_{\mathrm{m}}-h_{\mathrm{f}}}{h_{\mathrm{fg}}}$, X_{d} is the quality at the point of bubble departure, $h_{\mathrm{m}}$is the enthalpy of

mixture [J/kg], h_f is the enthalpy of saturated liquid [J/kg], h_{fg} is the heat of vaporization [J/kg].

The quality at the point of a bubble departure is obtained by

$$X_d = -\frac{C_p \cdot \Delta T}{h_{fg}}, \tag{12}$$

$$\Delta T = \frac{q'}{P_h \cdot h} - Q \cdot Pr \cdot Y_b \quad 0 < Y_b \leqslant 5, \tag{13}$$

$$\Delta T = \frac{q'}{P_h \cdot h} - 5Q \cdot \left(Pr + \log\left(1 + Pr\left(\frac{Y_b}{5} - 1\right)\right)\right) \quad 5 < Y_b \leqslant 30, \tag{14}$$

$$\Delta T = \frac{q'}{P_h \cdot h} - 5Q \cdot \left(Pr + \log(1 + 5Pr) + \frac{1}{2}\log\left(\frac{Y_b}{30}\right)\right) \quad Y_b > 30, \tag{15}$$

$$Q = \frac{q'}{P_h / v} C_p \cdot \sqrt{t_w \cdot v}, \tag{16}$$

$$t_w = \frac{f \cdot v}{8}\left(\frac{\dot{m}}{A_f}\right)^2, \tag{17}$$

$$Y_b = \frac{0.015}{\mu}\sqrt{\frac{\sigma \cdot D_h}{v}}, \tag{18}$$

where ΔT is the saturation temperature minus the local bulk fluid temperature [K], C_p is the specific heat [J/kg-K], h is the heat transfer coefficient [W/m^2-K], P_h is the wetted perimeter [m], Pr is the Prandtl number, q' is the local linear heat generation rate [W/m], Q is the non-dimensional heat input, Y_b is the distance from wall corresponding to tip of vapor bubble [m], τ_w is the wall shear stress [Pa], f is the friction factor, σ is the surface tension [N/m], A_f is the flow area [m^2], μ is the dynamic viscosity [kg/m-s], $\dot{m}$ is the mass flow rate [kg/s], v is the specific volume [m^3/kg], D_h is the hydraulic diameter [m].

From the true quality, void fraction, α, can be specified by a homogeneous model such as

$$\alpha = 0 \quad X_t \leqslant 0, \tag{19}$$

$$\alpha = \frac{X_t \cdot v_g}{(1 - X_t) \cdot v_f + X_t \cdot v_g} \quad X_t > 0, \tag{20}$$

where v_f is the specific volume of saturated liquid [J/kg-K], v_g is the specific volume of saturated vapor [J/kg-K].

It has been observed experimentally that the presence of boric acid in the coolant slows down the Zircaloy corrosion kinetics. It is proposed that H_3BO_3 in combination with LiOH might form a complex salt that appears to plug pores in the oxide and thereby effectively prevents the development of deep pores [17]. The corrosion resistance by boron is treated by adopting the Billot's factor of 0.64 [2] in the condition that lithium coupled with the void in the coolant affects the corrosion kinetics. So the boron effect on the corrosion behavior is expressed by

$$F_B = 0.64 \quad \text{if } \alpha \geqslant \alpha_0 \text{ in the presence of boron}, \tag{21}$$

$$F_B = 1.0 \text{ otherwise}. \tag{22}$$

3. Verification of developed model

The developed corrosion model is implemented into the fuel performance code, COSMOS [6,7] and then verified and qualified by using various fuel rods irradiated in different PWRs. We used the axial oxide thickness profile data measured at the end of the life of the fuel rods.

3.1. Case 1

Forty fuel rods covering extensive experiences of corrosion were selected for benchmarking the developed corrosion model. The benchmarking fuel rods with various claddings of Zircaloy-4 were irradiated under typical PWR conditions. The burnup of the fuel rods ranged from 10 MWd/kgU (energy generation in MW-day per uranium metal of 1 kg) to 60 MWd/kgU and the rod average linear heating rate reached up to ~270 W/cm. The Zircaloy-4 cladding contained the Sn contents of 1.22–1.58 wt%. A summary of the database of the fuel rods is listed in Table 1.

The inputs were rigorously prepared based on the measured values: geometrical fuel rod dimensions, metallurgical parameters of cladding, rod power with axial and radial power peaking factor, thermo-hydraulic conditions and the water chemistry. However, some measured data – for example, annealing parameters of several claddings – was not available so the related data was assumed to be the representative values of Zircaloy-4.

The measured oxide thickness for the forty benchmarking fuel rods was compared with the results by the COSMOS code. The comparison was performed for the axial profile of oxide and peak oxide thickness.

With the proper preparation of the inputs and the qualified corrosion model, the axial profiles of the oxide thickness were predicted at the peak position of the oxide. One example of the predictions is shown in Fig. 5 for the first rod in Group-A in Table 1. The reasonable prediction along the axis demonstrates the qualification of the developed model and its parameters.

In addition, the predictions by COSMOS at peak oxide thicknesses were compared to measured data in Fig. 6. The two dashed lines next to exact prediction – solid lines – represent the uncertainty of ±20 μm. This uncertainty can be explained from the following viewpoints:

(1) Since the corrosion process has a stochastic nature, different oxide thickness is inevitably observed even in sibling fuel rods which were fabricated by the same method and irradiated under the same operating conditions.

Table 1
Summary of fuel rods for benchmark database

	Rod number	Rod average burnup (MWd/kgU)	Average linear heating rate (W/cm)	Sn content (%)	Annealing parameter (h)
Group-A	6	40–60	~200	1.38–1.58	3×10^{-18}–8×10^{-18}
Group-B	6	40–50	250–270	1.22–1.54	8×10^{-18}
Group-C	16	35–50	120–250	1.38	6×10^{-19}–8×10^{-18}
Group-D	12	10–50	150–200	1.36–1.55	8×10^{-18}

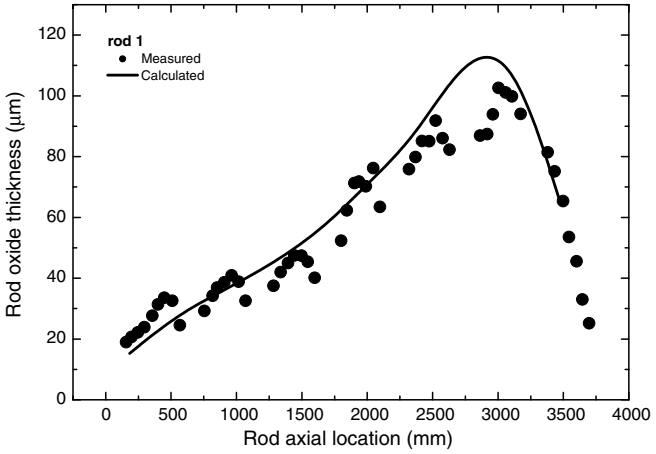

Fig. 5. Variation of the measured and predicted oxide thickness for Rod-1 of Group A in Table 1.

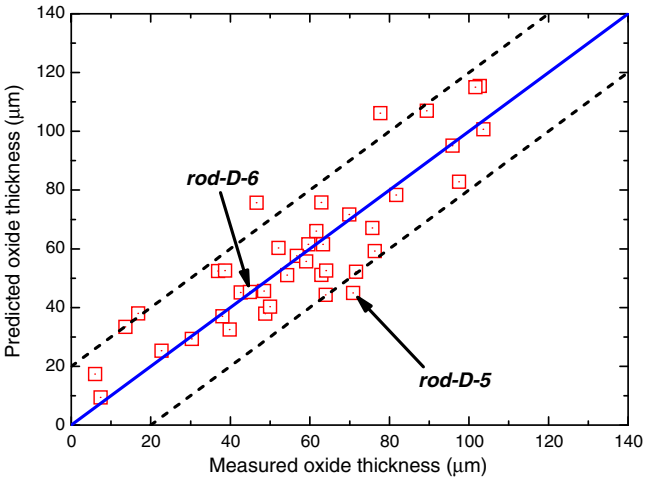

Fig. 6. Comparison between the measured and predicted oxide thickness for the benchmark rods.

(2) The COSMOS code, which was implemented with the present corrosion model and validated using many data, shows the uncertainty of about ±20 μm in predicting oxide thickness.

Therefore, it is expected that, when the COSMOS code is used to predict the oxide thickness, the estimated uncertainty would be ±20 μm. The overall prediction for the 40 fuel rods shows that the developed corrosion model is reasonable and proves that its parameters are properly selected although there are some scattered predictions lying outside the line of ±20 μm uncertainty. This discrepancy mainly comes from the observation of the oxide thickness variations between the side-by-side rods in an assembly, which is generally explained by inhomogeneity in the cladding or some other subtle variations of irradiation conditions.

For example, as shown in Fig. 6, rod-D-5 and rod-D-6 (the rods inclusive of Group-D in Table 1) used the same cladding and they were irradiated during three cycles with the burnup over 40 MWd/kgU. The measured oxide thickness of rod-D-5 was 71 μm whereas the value of rod-D-6 only reached 45 μm as indicated in Fig. 6. It is not clear why the discrepancy was observed between two sibling rods. The COSMOS code predicted the peak oxide thickness of 41 μm for both rods so the prediction by the COSMOS significantly deviates from the measured oxide thickness for rod-D-5 which exceeds more than 20 μm. However, it can be asserted that the developed corrosion model is appropriate if we consider the complicated corrosion behaviors in the different irradiation environments.

3.2. Case 2

A second database was selected to investigate the Sn effect and the water chemistry effect on the corrosion behavior in the fuel rods irradiated at a relatively high linear heat generation rate. Since a high heat generation rate induces unavoidable occurrence of subcooled boiling on the cladding surface, the water chemistry effect combined with the subcooled boiling can be explored properly.

Nine fuel rods irradiated in Grohnde PWR were used for the comparison between the measured and predicted oxide thickness.

Cladding materials were the reference and low Sn Zircaloy-4 with average Sn contents of 1.5 and 1.3 wt%, respectively [18]. The claddings were irradiated for 4 cycles, reaching 46 MWd/kgU with a nominal pH of 7.3. The maximum lithium hydroxide concentration was about 2.0 ppm at the beginning-of-the-cycle.

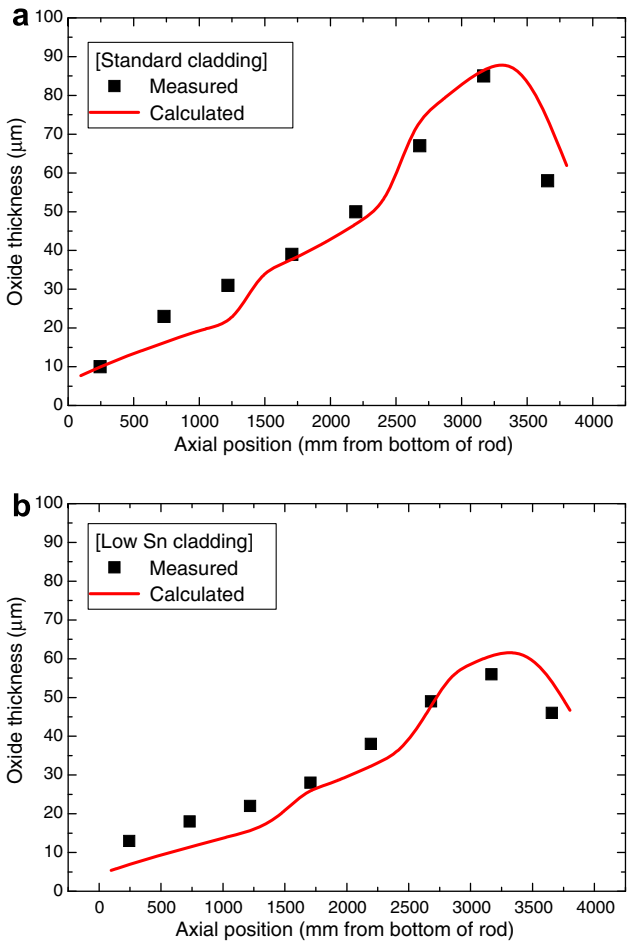

Fig. 7. Comparison of the calculated and measured oxide thicknesses for (a) standard cladding and (b) low Sn cladding.

Predicted oxide thickness for standard and low Sn claddings at the end of the cycle was compared with the measured data. Fig. 7 shows a typical comparison for the standard and low Sn claddings as a function of the axial rod position between the measured data and the calculated prediction. In these calculations, the fuel rod has been divided into 20 axial segments. As expected, the low Sn Zircaloy cladding is appreciably more corrosion resistant than the standard Zircaloy, i.e. the peak oxide layer thicknesses of the standard and low-Sn claddings were around 90 and 60 μm, respectively. The agreement between the measurements and the calculations is satisfactory for all nine fuel rods used for the calculation.

In addition, Fig. 8 shows results that illustrate the effect of the water chemistry on the corrosion behavior. Neglecting the water chemistry effect by bypassing the module for the subcooled void calculations leads to a discernable under-prediction, which ascertains that the lithium and boron concentrations with the void formation in the coolant can have an influence on the resultant corrosion kinetics. A good agreement is observed between the measured peak oxide thickness and the calculated values by considering the water chemistry enhancement. The lithium-induced corrosion acceleration is considered to result from the subcooled boiling on the cladding surface generated by a high linear heat generation rate. The predicted void fraction was substantial. This estimation confirms that it is reasonable to assume lithium enhancement in the condition of subcooled void formation.

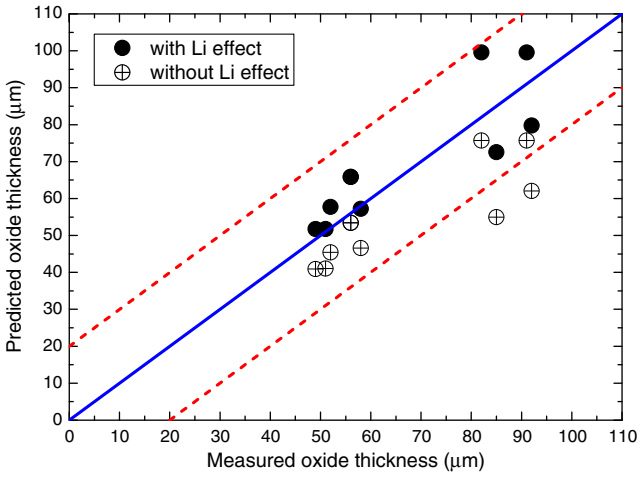

Fig. 8. Comparison of the oxide thicknesses showing the lithium effect.

3.3. Case 3

A third corrosion database was selected to clarify whether the lithium in the coolant can have an influence on the corrosion behavior even in the case of negligible void formation in the coolant.

Four fuel rods irradiated in Ringhals reactor were used for the verification. The Ringhals reactor is a 3-loop plant operating with 17 × 17 fuel assemblies at high LiOH concentrations (maximum 3.5 ppm). Cladding materials were the standard Zircaloy-4. The claddings were irradiated for 4 cycles, reaching approximately 40 MWd/kgU. Fuel rods with standard cladding were irradiated at a low heat generation rate, which means there was a negligible subcooled boiling.

The comparisons between the predicted and measured data for the end-cycle peak oxide layer thickness indicate a sufficient agreement and a representative comparison is shown in Fig. 9. This comparison reveals that the lithium effect was negligible even though the lithium concentration of 3.5 ppm was slightly higher than that (~2 ppm) of the nominal plant. The lithium enhancement would be realized only when the lithium enrichment occurs with subcooled boiling on the cladding surface.

3.4. Case 4

Corrosion in MOX fuel rods was investigated to check on the possibility of the difference of the corrosion behaviors between the MOX and UO_2 fuel.

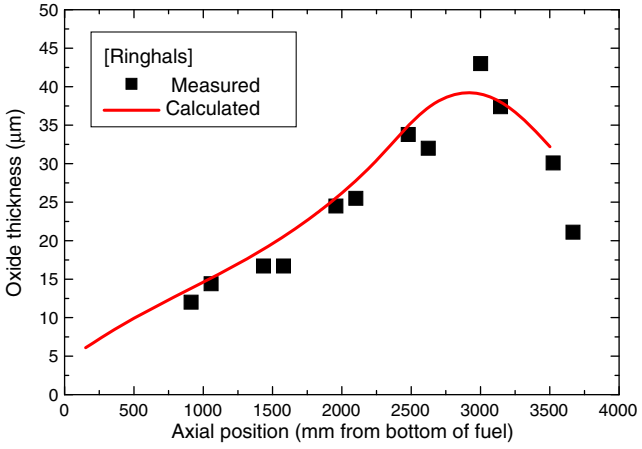

Fig. 9. Comparison of the calculated and measured oxide thicknesses from the database for the Ringhals reactor.

Two MOX fuel rods with the standard Zircaloy-4 cladding were irradiated in a PWR. The claddings were irradiated for 5 cycles, reaching the rod average burnup of 43 MWd/kgHM (energy generation in MWd per 1 kg of heavy metal (U,Pu) included in MOX fuels). Fuel rods with the standard cladding were irradiated at a low linear heat generation rate, which means there was a negligible subcooled boiling.

Fig. 10 shows the measured and calculated oxide thickness along the fuel rod. Both rods were irradiated at the similar conditions. They were therefore expected to have a similar oxide thickness but it was observed that oxide thickness was 41 μm in Rod-1 and 30 μm in Rod-2. There is a discrepancy in Rod-2 whereas the prediction is reasonable for Rod-1 along its axis at the end of the cycle. The discrepancy in Rod-2 can be explained in that two sibling rods had similar (even same) irradiation conditions but they had different oxide behavior due to the inhomogeneity of cladding or some other complexity. The lithium effect was negligible due to a low heating rate in the fuel rod. Furthermore, as expected, the comparison indicates no difference in the corrosion behavior between the MOX and UO_2 fuel [19].

Two other MOX rods were examined to consider the possibility of the difference in the corrosion behaviors between the MOX and UO_2 fuel for the higher fuel burnup. The two fuel rods investigated were located in the same fuel assembly of a commercial PWR. The assembly was irradiated for 4 cycles. Cladding material was Zircaloy-4 which contains the Sn content of 1.39–1.5%. The average linear heating rate during the four cycles ranged from 190 to 200 W/cm for the rods. The data for the base irradiation was obtained, including the power history, axial power and burnup distribution. The rod average burnup reached approximately 50 MWd/kgHM (energy generation in MW-day per heavy metal (U,Pu) of 1 kg).

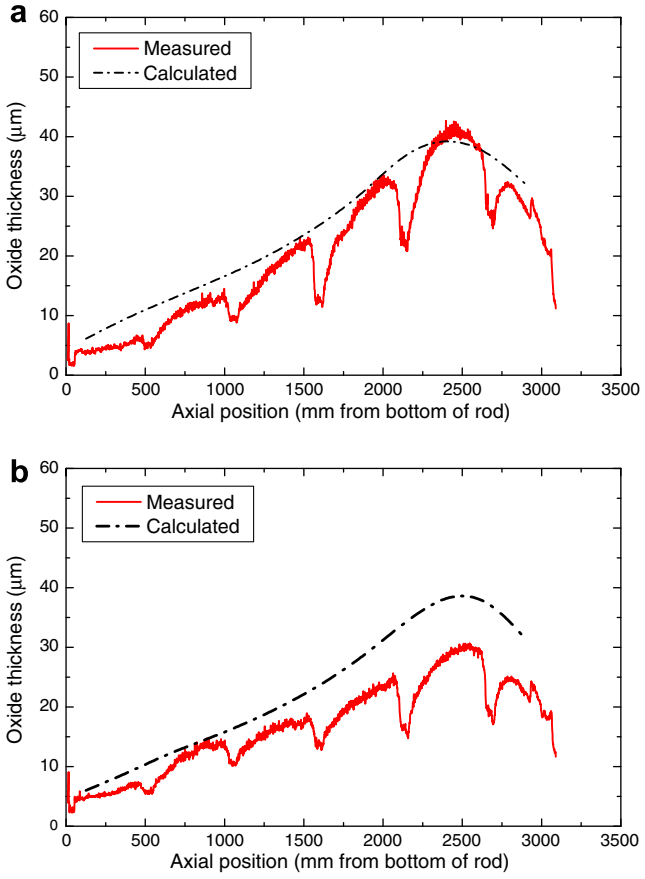

Fig. 10. Comparison between the calculated and measured oxide thickness for the MOX fuel (a) Rod-1 and (b) Rod-2.

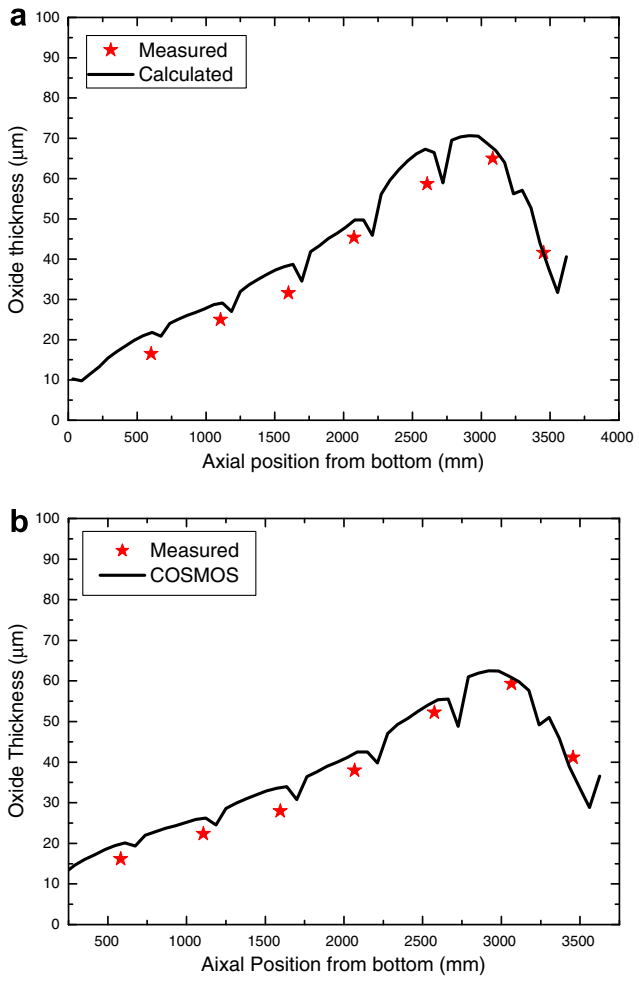

Fig. 11. Comparison between the measured and calculated oxide thickness of (a) Rod-1 and (b) Rod-2 cladding after a base irradiation in a PWR.

After the irradiation, a post irradiation examination (PIE) was performed, which enabled us to confirm the applicability of the COSMOS code for the oxidation of high burnup MOX rods. The measured oxide thickness is compared with the prediction by the COSMOS code. Fig. 11 shows the oxide thickness measured after base irradiation, together with the predicted values by the COSMOS. Measured oxide thickness profile is obtained from averaging along four angular orientations. The peak oxide thicknesses are approximately 60–70 μm at the sixth span. Both rods show a significantly reduced oxidation between the spacer grids. Comparison between the measured and calculated oxide thickness along the axis confirms the appropriateness of the corrosion model in the COSMOS code, up to the high burnup of MOX fuels.

4. Conclusions

A phenomenological corrosion model for various Zircaloy-4 cladding in PWRs was developed to consider the metallurgical effect of cladding and the water chemistry effect coupled with the thermo-hydraulic condition of the coolant. The effects of the Sn content and the annealing parameter were formulated by analyzing measured corrosion data. Concerning the water chemistry effect, it was assumed that lithium and boron have an influence on the corrosion behavior in the condition of subcooled void formation on the cladding surface.

The developed corrosion model was implemented into the fuel performance code, COSMOS, and verified with the cladding corrosion data of four cases.

The prediction for the extensive database on 40 fuel rods revealed that the corrosion model was developed properly to estimate corrosion behaviors under various PWR conditions. The lithium enhancement effect on corrosion behavior was elucidated from the fuel rods irradiated at a high linear heat generation rate so the significant subcooled void could be formed on the cladding surface. However, the cladding irradiated under the slightly higher lithium concentration but with negligible subcooled void formation did not indicate any enhancement of its corrosion. These corrosion behaviors manifest the acceleration of corrosion by lithium enrichment only coupled with the subcooled void formation on the cladding surface. In addition, the developed corrosion model indicates no difference in the corrosion behavior between MOX and UO_2 fuels which is consistent with the measured corrosion behaviors.

Agreement between the predicted oxidation behaviors with the measured data shows the appropriateness of the COSMOS code to estimate the cladding oxidation.

Acknowledgements

The authors would like to express their appreciation to the Ministry of Science and Technology (MOST) of the Republic of Korea for the support of this work through the mid- and long-term nuclear R&D Project. We also want to thank D.H. Hwang and Y.J. Yoo for their provision of subroutines to estimate the proper void fraction in the coolant. In addition, we are grateful to FIGARO committee, NOK and Siemens Power Corporation for the delivery of the relevant corrosion database.

References

[1] S.H. Shann, L.F. Van Swam, L.A. Martin, in: Proceedings of the International Topical Meeting on LWR Fuel Performance, Avignon, France, 1991, p. 742.
[2] P. Billot, J. Robin, A. Giordano, J. Peybernes, J. Thomazet, H. Amaulrich, in: A.M. Garde, E.R. Bradley (Eds.), Zirconium in the Nuclear Industry: Tenth International Symposium, ASTM STP, 1245, American Society for Testing and Materials, Philadelphia, 1994, p. 351.
[3] T. Kido, K Ranta-Puska, OECD Halden Reactor Project Report, HWR-333, 1992.
[4] T. Karlsen, C. Vitanza, in: A.M. Garde, E.R. Bradley (Eds.), Zirconium in the Nuclear Industry Tenth International Symposium, ASTM STP, 1245, American Society for Testing and Materials, Philadelphia, 1994, p. 779.
[5] M.V. Polley, H.E. Evans, P.O. Andersson, J. Larsson, EPRI Report, EPRI TR-100389, Project 2493-5, 1992.
[6] B.H. Lee, Y.H. Koo, J.Y. Oh, J.S. Cheon, D.S. Sohn, Nucl. Technol. 157 (2007) 53.
[7] W. Wiesenack, B.H. Lee, D.S. Sohn, Nucl. Eng. Technol. 37 (2005) 317.
[8] W.H. Press, B.P. Falnnery, S.A. Teukolsky, W.T. Vetterling, Numerical Recipes in Fortran 90, Cambridge University Press, 1986.
[9] IAEA-TECDOC-996, Waterside corrosion of zirconium alloys in nuclear power plants, IAEA, 1998.
[10] Otto A. Besch, S.K. Yagnik, K.N. Woods, C.M. Eucken, E.R. Bradley, in: E.R. Bradley, G.P. Sabol (Eds.), Zirconium in the Nuclear Industry: Eleventh International Symposium, ASTM STP, 1295, American Society for Testing and Materials, Philadelphia, 1996, p. 805.
[11] B. Cheng, P.M. Gilmore, H.H. Klepfer, in: E.R. Bradley, G.P. Sabol (Eds.), Zirconium in the Nuclear Industry Eleventh International Symposium, ASTM STP, 1295, American Society for Testing and Materials, Philadelphia, 1996, p. 137.
[12] P. Billot, A. Giordano, in: C.M. Eucken, A.M. Garde (Eds.), Zirconium in the Nuclear Industry: Ninth International Symposium, ASTM STP, 1132, American Society for Testing and Materials, Philadelphia, 1991, p. 539.
[13] M. Noe, P. Beslu, J. Thomazet, IWGFPT/24, IAEA, Vienna, 1986, p. 70.
[14] S. Levy, Int. J. Heat Mass Transfer 10 (1967) 951.
[15] C.L. Wheeler, C.W. Stewart, R.J. Cena, D.S. Rowe, A.M. Sutey, BNWL-1962, BATTELLE Pacific National Lab., 1976.
[16] D.H. Hwang, Y.J. Yoo, W.K. In, S.Q. Zee, Nucl. Eng. Des. 199 (2000) 257.
[17] B. Cox, M. Ungurelu, Y.M. Wong, C. Wu, in: E.R. Bradley, G.P. Sabol (Eds.), Zirconium in the Nuclear Industry: Eleventh International Symposium, ASTM STP, 1295, American Society for Testing and Materials, Philadelphia, 1996, p. 114.
[18] A.R. Massih, P. Rudling, in: Proceedings of the ANS International Topical Meeting on Light Water Reactor Fuel Performance, Avignon, France, 1991, p. 716. April 21–24.
[19] P. Schleuniger et al., Final report on NDT, Puncture and Sample Cutting, FIG 99/18, BN. REF. 9905318/221, 1999.